Large-Area Plasmonic-Crystal−Hot-Electron-Based Photodetectors

F. Pelayo García de Arquer, Agustín Mihi,* and Gerasimos Konstantatos*

ICFO - Institut de Ciències Fotòniques, Mediterranean Technology Park, 08860 Castelldefels, Barcelona, Spain

S *Supporting Information*

ABSTRACT: In view of their exciting optoelectronic light−matter interaction properties, plasmonic−hot-electron devices have attracted significant attention during the last few years as a novel route for photodetection and light-energy harvesting. Herein we report the use of quasi-3D large-area plasmonic crystals (PC) for hot-electron photodetection, with a tunable response across the visible and near-infrared. The strong interplay between the different PC modes gives access to intense electric fields and hot-carrier generation confined to the metal−semiconductor interface, maximizing injection efficiencies with responsivities up to 70 mA/W. Our approach, compatible with large-scale manufacturing, paves the way for the practical implementation of plasmonic−hot-electron optoelectronic devices.

KEYWORDS: *hot carriers, plasmonic crystal, photodetectors, soft nanoimprint lithography, internal photoemission*
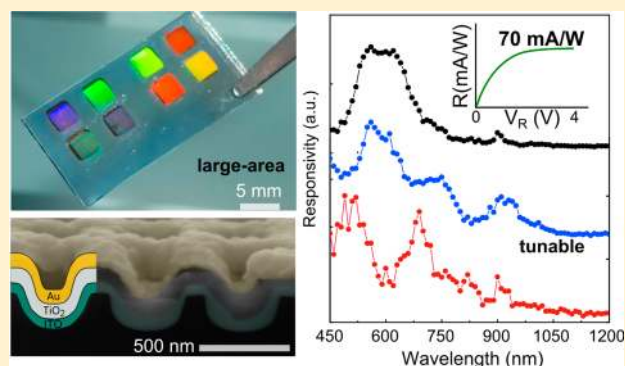
The unique light−matter interaction properties endowed by the plasmonic character of free electrons in metallic nanostructures have motivated vivid research that during the last few decades found applications in a variety of fields such as biology,[1] chemistry,[2] medicine,[3] information theory, and quantum optics[4−6] or energy harvesting and photodetection.[7−9]

These plasmonic resonances give rise to photocurrent generation by decaying into highly energetic electrons, so-called "hot electrons", which are then emitted from the metal before thermalization and collected at the electrodes on the basis of the principle of internal photoemission.[10,11] The field of hot-electron plasmonics has rapidly developed during the last years,[11−33] led by the interest in active optoelectronic devices with functionalities that emanate from their plasmonic character, such as a tailored spectral response, which are especially appealing for solar-energy harvesting,[11−19] and subband-gap visible or infrared detection.[20−27] The increase in hot-electron-based devices has also been fostered by the advances in associated nanofabrication technologies. Electron or ion-beam lithographies are currently used to fabricate prototypes that exploit the spectral tunability of plasmonic architectures. These devices have relied on nanoparticles,[11,22] nanoantennas,[12,20,26] or gratings[24] to excite individually either localized plasmons or surface plasmon polaritons, whose relaxation eventually leads to the creation of hot carriers. This nanostructuring, required to address the spectral tunability in these devices, has hitherto relied on low-throughput, costly, and time-consuming lithographic processes. This may seriously limit the future potential of plasmonic−hot-electron optoelectronics because large-area and high-throughput manufacturing are requisites for energy-harvesting and large-area optoelectronic applications.[34] Here we report the implementation of

plasmonic crystals (PC) as a novel platform for hot-electron generation.[35,36] PCs, similar to their dielectric counterparts (photonic crystals), are periodically organized metallic architectures that present tunable optical responses by slight variations of their periodicity or topology, providing an excellent platform to control the bandwidth and operational regime of our hot-electron-based photodetectors.[37] The use of PCs allows for the concurrent excitation of different modes: those of the individual unit cells (localized surface plasmons), the ones derived from the periodic nature of the film (lattice modes), or the resulting strong interaction between them (hybrid modes).[38] We exploit herein this versatile platform for hot-electron-based photodetection. By employing this architecture, we were able to fabricate photodetectors with a tunable and multiband spectral response across the vis−NIR spectrum. By tailoring the mode interplay, we are able to access intense plasmonic resonances that with a confined hot-electron generation within a metal mean-free-path distance to the interface result in maximized hot-electron injection and responsivities up to 70 mA/W under applied bias. In this work, we provide an in depth analysis of the optical response of the architectures and the electrical performance of the derived photodetectors. Unlike in prior plasmonic−hot-electron devices, the fabrication of our detectors relies on soft nanoimprinting lithography (NIL):[39] a low-cost, large-area, and high-throughput nanostructuring technique that has already shown promising applications for surface enhanced Raman spectroscopy[36,37] and photovoltaic light trapping among others.[34,40,41] Our approach paves the way for the implementa-
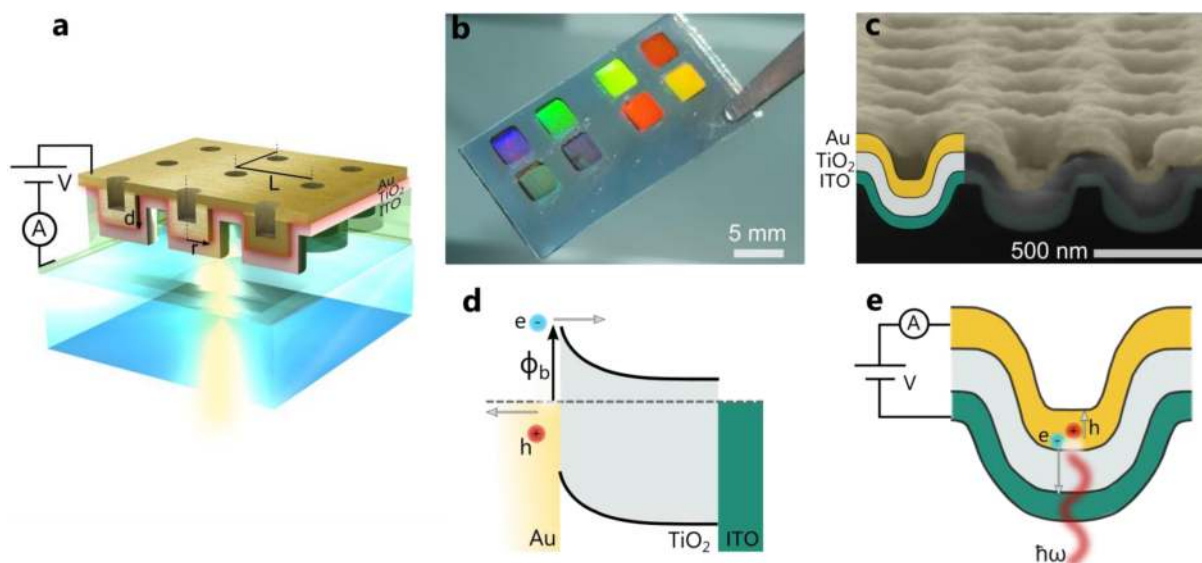
Figure 1. Device architecture and principle of operation. (a) Representation of the plasmonic crystal photodetector. Light impinges from the bottom (ITO/glass), exciting resonant modes responsible for hot electron generation. The plasmonic crystal is defined by the lattice parameter L, pillar radius r, and depth d. Depending on those parameters, the light-interaction properties can be tailored, as illustrated in the photograph of a substrate containing eight 9 mm^2 devices; the reflected colors are indicative of the nanostructured metal electrodes. (c) Cross-sectional SEM artificially colored to portray the different layers of the architecture. (d) Excited hot electrons are collected in the presence of the resulting Schottky junction, characterized by an effective barrier Φ_b. (e) Resulting photodetector.

tion of the proposed architecture on a large-scale for a vast variety of optoelectronic devices.

RESULTS

The plasmonic crystal photodetector is fabricated as follows: first, a 2D square array of cylinders is shaped in a photoresist via soft nanoimprinting using a prepatterned PDMS (polydimethyl-siloxane) mold.[39] Next, an indium-doped tin oxide (ITO) layer is sputtered, followed by a conformal TiO$_2$ coating and an ultrathin layer of alumina. The role of this layer has been previously reported[15] as a means of interface passivation with the associated reduction in dark current for photodetectors (Supporting Information section S1). On top of this, a gold metal film is deposited to finally result in a quasi-3D plasmonic crystal defined by the lattice parameter (L), gold pillar radius (r), and depth (d). (See Methods and Supporting Information section S2.) The final architecture of the PC-based photodetector is represented in Figure 1a. When illuminated from the bottom (glass/ITO), plasmonic resonances excited in the corrugated gold (also acting as top counterelectrode) decay into hot electrons that are injected into the TiO$_2$ layer and eventually collect at the ITO electrode. Several 9 mm^2 devices of different geometric characteristics were fabricated (r = 35 nm and L = 450 nm, r = 85 and L = 450 nm, and r = 35 and L = 550 nm). A photograph of an ITO-coated glass containing eight devices is shown in Figure 1b. The intense colors observable with the naked eye result from the different diffracted orders associated with the periodicity of each device. A cross-sectional scanning electron micrograph (SEM) of a device is shown in Figure 1c, where the conformal gold, titania, and ITO layers on the imprinted photoresist can be identified. The optoelectronic operation of our photodetector builds on the interaction of the quasi-3D plasmonic crystal with light: Photons, impinging from the ITO side, excite different modes in the metal. These resonances eventually lead to the creation of a population of hot electrons within its conduction band

(Figure 1d). The energetic hot electrons are then harvested by the electric field of the Schottky barrier, of height Φ_b, that is present at the Au−TiO$_2$ interface. In this way, electrons that are injected to the TiO$_2$ are collected through the ITO (Figure 1e), giving rise to a photocurrent dictated by the different resonances of the plasmonic crystal.[20]

The tunability of the proposed architecture is illustrated in Figure 2a,b, where a map of the absorption in the Au electrode is shown as a function of wavelength and lattice parameter L for the two metallic cylinder radii under consideration: r = 35 nm (Figure 2a) and r = 85 nm (Figure 2b) as simulated by FDTD. (See details in the Supporting Information section S3.) As described in ref 42, the interaction of light with the plasmonic crystal network can be understood in terms of the polarizability of the individual building blocks α and their coherent interplay facilitated by the lattice G. The induced electrical dipole p in the structure can be represented as

$$p = \frac{1}{1/(\alpha(r, d, \lambda) - G(L, \lambda))} E_{\text{ext}} \qquad (1)$$

where E_{ext} is the external electric field.[42] These 2D maps help identify the type of plasmonic modes excited in the structure, namely: (i) Bragg−SPP modes, depending only on the diffraction condition imposed by the lattice parameter (L) as described by G, (ii) localized modes within each unit cell (in our case, a cylindrical metal pillar surrounded by different semiconducting shells) that are L-invariant, and (iii) the coupling of the collective lattice modes (i) with the individual resonances of (ii) that result in very strong hybrid resonances because the denominator in eq 1 tends to zero.[43−45]

When the PC is composed of small cylinders of 35 nm radius (Figure 2a), lattice modes dominate above λ = 850 nm. In the λ = 600−800 nm region, the SPP and the resonances of the pillars interact with each other, giving rise to strong hybrid modes intensifying the absorption of the gold at this energy range. Below λ = 500 nm, interband absorption in the gold is
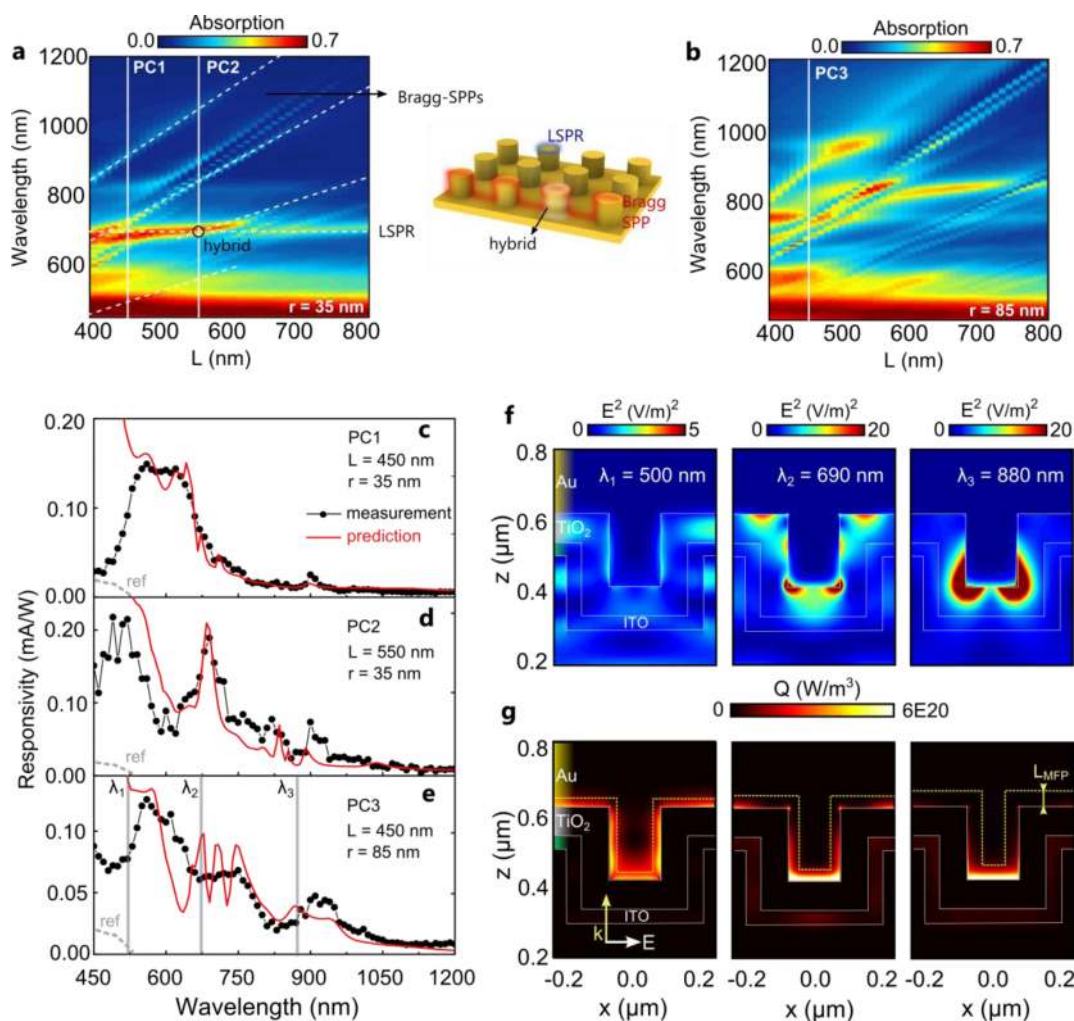
Figure 2. Plasmonic-crystal−hot-electron-based photodetection. Absorption in the plasmonic crystal as a function of wavelength and lattice parameter for the different metal cylinders under consideration r = (a) 35 nm and (b) 85 nm. These 2D maps help identify the type of plasmonic modes excited in the structure, viz.: (i) Bragg−SPP modes, depending only on the diffraction condition imposed by the lattice parameter (L), (ii) localized modes within each unit cell (L-invariant), and (iii) their interaction. Experimental responsivity for different plasmonic crystals: (c) L = 450 nm and r = 35 nm, (d) L = 550 nm and r = 35 nm, and (e) L = 450 nm and r = 85 nm. The theoretical responsivity, calculated from eq 2, is overplotted in each graph with red solid lines. The responsivity of a flat reference sample is shown for comparison. (f) Simulated electric-field intensity cross-sectional maps for the PC3 device at the wavelengths indicated in e. (g) Corresponding hot-electron generation rate (Q). The dashed line represents the mean free path for each wavelength.

predominant, yet diffracted orders contribute to increase absorption. By increasing the radius of the pillars (Figure 2b, r = 85 nm), the individual resonances are overall shifted toward the near-infrared, reshaping the map of the resulting modes. (See also Supporting Information section S4.) The strong mode interaction is evidenced by intense absorption and anticrossing features[42,43] appearing when lattice and localized resonances coincide (e.g., L = 510 nm and λ = 960 nm). This results in different hybrid modes within the λ = 600−1000 nm region, extending well the absorption of gold up to 1000 nm. Further evidence of mode interaction is given by the angle-dependent absorption, showcasing their different contribution across the vis−NIR spectrum. (See details in Supporting Information section S5.)

We then sought to experimentally assess the optoelectronic spectral response of plasmonic crystal photodetectors of different L and r. At a first approximation, the responsivity of these devices $R(\lambda)$ is expected to follow the absorption in the plasmonic crystal $A(\lambda)$, modified by the amount of electrons at

each energy capable of overcoming the Schottky barrier as predicted by the Fowler theory:[46]

$$R(\lambda) = C\frac{(\hbar\omega - \Phi_b)^2}{\hbar\omega}A(\lambda) \qquad (2)$$

where C is a fitting coefficient,[47] $\hbar\omega$ is the energy of the incident photon, and Φ_b is the effective Schottky barrier height, which we estimated to be 0.68 eV from current−voltage measurements. (Full details on this calculation can be found in Supporting Information section S6.) The responsivity, measured under short-circuit conditions, is shown in Figure 2c−e. For L = 450 nm and r = 35 nm (Figure 2c, PC1), a broad band and intense response is obtained between λ = 500 and 700 nm, originating from the overlap of the different hybrid modes in this region. A weaker, narrower resonance appears at λ = 900 nm, corresponding to a lattice resonance of the plasmonic crystal. Below λ = 500 nm, predicted and experimental responsivities diverge as a consequence of the increasing contribution of the interband transitions, which

would yield lower energy electrons, and the shorter electron mean free path.[48,49] The responsivity of the device that is based on a plasmonic crystal with $L = 550$ nm (Figure 2d, PC2) shows different clear peaks, around $\lambda = 500, 700, 800$, and 900 nm. The origin of these peaks can be associated with the resonances indicated by a vertical solid line in Figure 2a. The first resonance, at $\lambda = 500$ nm, corresponds to the overlap of a lattice, Bragg mode, with the bulk gold absorption. As a consequence, generated hot electrons are expected to be located within the side of the cylinder and along a larger energy span.[50] This is in contrast to PC1, which displays a dip in responsivity despite the prominent contribution of interband transitions. For $\lambda = 700$ nm, localized and lattice modes give rise to a strong and narrow resonance. The peaks at longer wavelengths correspond to different lattice modes. Finally, the responsivity of the photodetector that is based on PCs with $L = 550$ nm and $r = 85$ nm is shown in Figure 2e (PC3). A clear set of three broad resonances in the responsivity spectrum up to 1 μm is obtained as a consequence of the different resonant modes excited with this crystal configuration. The predicted responsivity profile, calculated from eq 2, is shown in each graph as a solid red line. The absorption spectra correspond to the vertical solid lines indicated in Figure 2a,b (PC1, PC2, and PC3).

To gain insight into the nature of the different resonances and its implications for the hot-electron generation and collection process, we calculated the electric-field intensity profiles (Figure 2f) and the generation rate profile Q, (Figure 2g), defined as

$$Q(x, z, \lambda_i) = \frac{1}{2}\omega \, \text{Im}(\varepsilon(x, z, \lambda_i))|E(x, z, \lambda_i)|^2 \tag{3}$$

for different modes. The field intensity profile for $\lambda_1 = 500$ nm spreads within the TiO$_2$ layer and the photoresist and extends into the metal plate and cylinder. The corresponding hot-electron generation spreads within the volume of the gold pillar (Figure 2g, left), but only a fraction of it is within a mean-free-path distance to the interface (15−20 nm).[51] This, in combination with the increasing interband contribution at these energies, accounts for the difference between the experimental and predicted responsivities in this wavelength range.

The resonance at $\lambda_2 = 690$ nm (Figure 2f, middle) presents clear high-intensity nodes bound to the Au/TiO$_2$ interface. In this case, the pillar cavity is in resonance with a lattice mode, which allows for the excitation of resonances along the cylinder wall and gives rise to much stronger electric fields reaching inside the metal. The hot-electron generation profile at this wavelength is strongly localized within the bottom of the pillar and mostly within the range defined by the mean free path (around 30 nm). It is therefore expected that this mode profile contributes more to the photocurrent of the device.

For $\lambda_3 = 880$ nm (Figure 2f, right), the electric-field intensity is highly localized in the bottom of the Au pillar, with less penetration inside the metal. The resulting generation profile is even more confined in this case, which in combination with the more intense electric fields leverages the lower injection rates otherwise expected for electron energies into the NIR regime.[48]

The optoelectronic response of the presented architecture can be further tailored by modifying other structural or material parameters. The refractive index of the semiconductor can be, for example, used as a leverage to tailor the spectral absorption. For a fixed geometry, this results in a metal absorption

tunability, which spans across the vis−NIR spectrum, also showcasing the potential of these devices as a tool for active optoelectronic material sensing (Figure 3, left column).
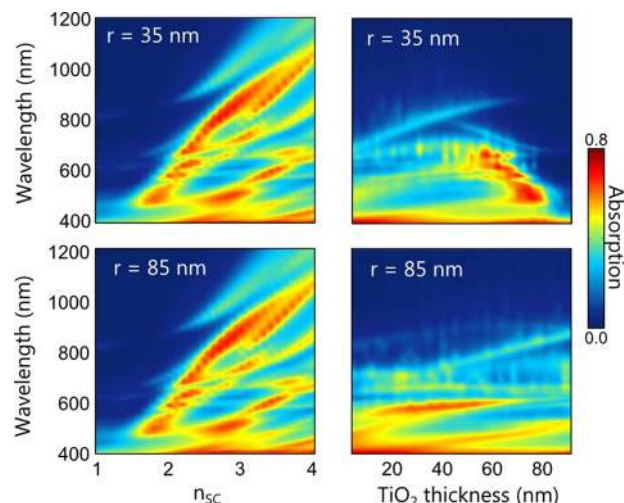

Figure 3. Modification of the semiconductor refractive index (left column) and thickness (right column) as a design parameter. By varying the refractive index of the semiconductor, the response of the photonic crystal can be tailored across the VIS-NIR. Alternatively, this architecture can be used to actively measure changes in the refractive index. If the thickness of the semiconducting layer is modified, then the optical response changes as a consequence of the different fill factor.

Variations in the TiO$_2$ coating thickness, and hence in the associated photonic crystal fill factor, can also be used as design parameter to tune the spectral response (Figure 3, right column).

We now turn to the optoelectronic characteristics of these structures as photodetectors. The dark-current voltage response, indicative of a Schottky junction between Au and TiO$_2$, is shown in Figure S6. Despite the high tunability offered by our plasmonic crystal architecture, responsivities under short-circuit conditions are still low for practical applications, a common drawback for plasmonic−hot-electron devices. The application of a reverse bias to the Au/TiO$_2$ junction, however, could in principle allow overcoming of the low injection yield because the associated decrease in the barrier height favors an increasingly efficient hot-electron injection. (See scheme depicted in Figure 4.) Initially, the hot electron population spans between E_f and $E_f + \hbar\omega$ with a density described as $N(E) = f(E) \, g(E)$ (where $g(E)$ is the density of states in the conduction band of the metal and $f(E)$ is uniform along $[E_f, E_f + \hbar\omega]$. Under short-circuit conditions, only the fraction of those hot electrons that can reach the interface with enough momentum are tunneling candidates. We described this process by considering the energy-dependent mean free path and field profile as described in Supporting Information section S7. The situation changes under the application of a reverse voltage (V_R) as the barrier is modulated (Figure 5c): Depending on the how the voltage drops across the Al$_2$O$_3$ and TiO$_2$ layers ($V_{0,\text{ins/sc}}$ at 0 V and increasing as determined by the series resistance contribution of alumina γ), the barrier profile is modulated as their conduction bands are pushed downward, facilitating injection ($p_{inj} = p_i p_v$ where p_t is the tunneling probability). As the reverse bias approaches $\hbar\omega$, the injection
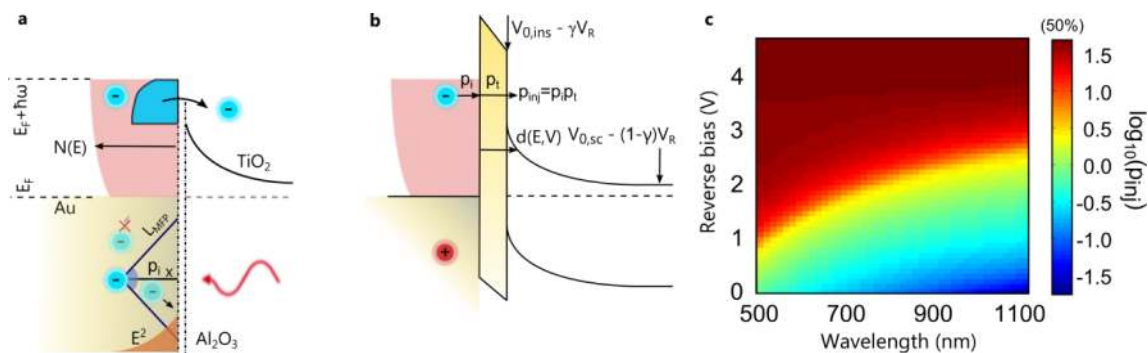
Figure 4. Hot-electron injection and barrier modulation. (a) Initially, the hot-electron population spans between E_F and $E_F + \hbar\omega$ with a density described as $N(E)$. The hot-electron injection at short-circuit conditions is limited by the fraction of those that can reach the interface with enough momentum (blue-shaded area). We have modeled this according to energy-dependent mean free path in the probability p_i. (b) The application of a reverse voltage (V_R) results in the modulation of the barrier: depending on the how the voltage drops across the Al_2O_3 and TiO_2 layers ($V_{0,ins/sc}$ at 0 V and increasing as determined by the series resistance contribution of alumina γ), their conduction bands are pushed downward, facilitating injection ($p_{inj} = p_i p_t$, where p_t is the tunneling probability). For more details, see Supporting Information section S7. (c) As the reverse bias approaches $\hbar\omega$, p_{inj} can be substantially improved reaching the 50% limit for half-space emission.
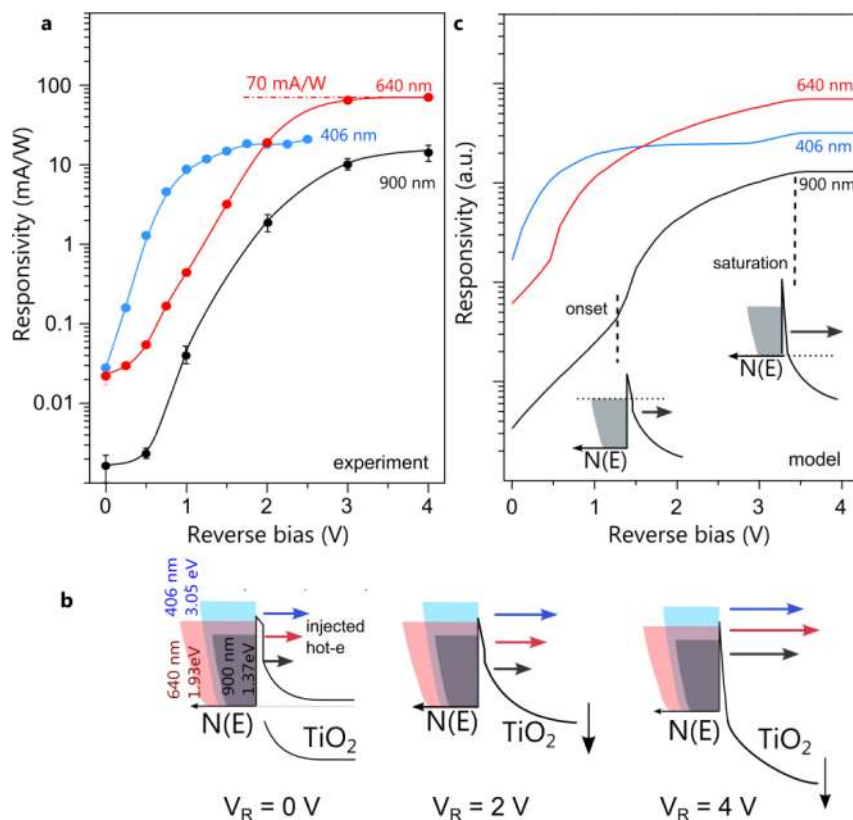

Figure 5. Device optoelectronic performance. (a) Responsivity as a function of applied reverse bias for a representative device ($r = 85$ nm and $L = 450$ nm) at three different illumination wavelengths. Reversely biasing the junction results in a prominent increase of responsivity as a higher fraction of the hot electron population is able to tunnel through the Al_2O_3/TiO_2 barrier. Depending on the illumination energy, different responsivity onsets and saturation voltages are obtained, as the tunneling probability increases for lower energies with increasing bias. A maximum $R = 70$ mA/W (yielding an estimated IQE of 27%, Supporting Information section S6) is obtained for 640 nm illumination at 4 V reverse bias. (b) Schematic of hot electron tunneling under reverse bias. As the reverse bias increases, the Al_2O_3/TiO_2 barrier is lowered, resulting in higher injection (depicted by the different arrows). (c) The experimental trends are in qualitative agreement with the analytical model describing hot-electron photocurrent for a bias-dependent barrier (Figure 4 and Supporting Information section s7). The onset and saturation voltages correspond to the situations depicted in the inset.

probability can be substantially improved, reaching the 50% half-space emission limit.

To experimentally assess this improvement, the device responsivity as a function of reverse bias is shown in Figure 5a for different illumination wavelengths. We observe that

absolute values are indeed increasing by orders of magnitude for increasing reverse bias. A higher fraction of the excited electrons can overcome the barrier, increasing responsivity as the reverse voltage increases. A similar behavior was also recently reported in MIM hot-electron devices.[26] Remarkably,

both responsivity onset and saturation features depend on the energy of the excitation $\hbar\omega$, as depicted for 406, 640, and 900 nm illuminations. As the hot electron population spans along E_f and $E_f + \hbar\omega$,[48,52] higher energy excitations are consequently expected to produce responsivity onsets and saturations at lower voltages. This trend is experimentally confirmed in our case, where both onset and saturation voltages clearly depend on the illumination wavelength (as illustrated in the scheme in Figure 5c). The observed trends are in agreement with the theoretical model of tunneling through a bias-dependent barrier introduced in Figure 4.

The situation of low performance under short-circuit conditions can therefore be overcome by operating the devices under reverse bias. In the saturation regime, responsivities as high as 70 mA/W are within reach, being ultimately limited by the absorption of the structure and the emission of hot electrons. The corresponding external quantum efficiency (ratio of collected carriers to number of incident photons) in this case is 12%, yielding an estimate (Supporting Information section S9) for the internal quantum efficiency of up to 27% (ratio of collected carriers to number of absorbed photons). Given the injection probability obtained for this configuration, a plasmon−hot-carrier-generation efficiency of approximately 54% is estimated for the hybrid mode (Table 1). The dynamic

Table 1. Responsivity, EQE, Simulated Absorption, and Estimated IQE for the Different Resonances

λ (nm)	R (mA/W)	EQE (%)	A (%)	IQE (%)
405 (Bragg + bulk)	19	5.8	60	9.6
640 (hybrid)	70	12	45	27
900 (SPP−Bragg)	11	1.6	35	4.5

range characteristics of our devices are showcased in Figure S9, where a linear response of the photocurrent as a function of incident power is shown, which suggests that within the collected electrons there are not nonlinear processes involved such as the collection of secondary excited electrons.

We present a robust and novel architecture for multispectral visible−infrared photodetection that is based on hot-electron injection from plasmonic crystals. Our approach combines the versatility of this platform, which allows us to tailor the optical response of the devices across the visible and near-infrared, with the large-area-compatible manufacturing enabled by soft nanoimprinting lithography. By tailoring the strong mode interaction between localized and lattice resonances, we manage to confine hot-electron generation within the metal mean free path. In such a way, a significant fraction of the excited carriers can be collected. Under reverse bias operation, our devices yield responsivities up to 70 mA/W and IQEs up to 27%. Under these conditions, this represents a significant performance improvement compared to prior reports in hot-electron photodetection,[27,28,53] making this platform a viable alternative for other well-established technologies for subband-gap photodetection that are based on internal photoemission, such as metal silicides (Supporting Information section S10).[54]

The variation of parameters such as the refractive index of the different PC constituent materials can potentially give access to other spectral regions, such as short- and midwavelength infrared, as an alternative to toxic HgCdTe-based photodetection[55] or even to long-wave infrared and THz.[56] Other areas such as photovoltaics or photocatalysis[31] can benefit from this architecture because it bridges the gap

between large area, infrared sensitization, and high performance. Further development might rely on the study of specific plasmonic crystals with tunable optical band gaps or on the exploitation of plasmonic nonlinear processes associated with intense electric fields.[5,57]

■ METHODS

Device Fabrication. Nanostructured electrodes were fabricated by nanoimprinting lithography. A polydimethylsiloxane mold (PDMS, 10:1 Sylgard 184) replicating a square array pattern from a silicon wafer (AMO gratings) was used as printing stamp. A UV-photocurable epoxy (SU8, Microchem) was spin-cast on top of ITO-coated substrates (Stuttgart University) to make 500 nm thick films. Samples were ethanol-wetted and imprinted with the PDMS stamp. After imprinting, patterned resists were UV cured through a spatial mask defining square-imprinted regions of 9 mm^2 to improve its mechanical stability (λ = 360 nm, 15 min). Once the resists were exposed and developed, 40 nm of ITO was sputtered onto the substrates using an AJA sputtering system without masking so that the sputtered ITO was electrically connected to the commercial ITO-coated substrate. Finally, a 90 min annealing step at 200 °C was carried out under inert atmosphere to improve the conductivity of ITO. A 60−80 nm layer of TiO$_2$ and a 0.5 nm layer of Al$_2$O$_3$ were deposited by atomic layer deposition as previously described.[15] A 200 nm layer of gold was deposited on a Kurt J. Lesker Nano 36 Systemat a rate of 0.5 Ås^{-1} for the first 30 nm and 1.5 Ås^{-1} for the remaining 250 nm. The base pressure was lower than 2×10^6 mbar. Finally, a 90 min anneal at 200 °C under inert atmosphere was carried out to improve the conductivity of ITO. Further fabrication details can be found in Supporting Information section S1 and elsewhere.[41]

TiO$_2$ and Al$_2$O$_3$. A 80 nm layer of TiO$_2$ and a 0.5 nm layer of Al$_2$O$_3$ were deposited by atomic layer deposition (Savannah 200, Cambridge Nanotech). The role of the alumina coating is to passivate defects present on the titania surface as described elsewhere.[15] Water and trimethylaluminum were used as precursors of Al$_2$O$_3$ with open valve times of 0.05 and 0.10s, respectively, followed by a 65 s pump time (1.1 A per cycle). The chamber was kept at 150 °C during the deposition process. TiO$_2$ coatings were fabricated from water and titanium isopropoxide; valves were set to 0.015 and 0.065 s, respectively, followed by a 10 s pump time (0.025 A per cycle). The deposition chamber temperature was held at 200 °C.

Metal Electrode. A 200 nm layer of metal was deposited on a Kurt J. Lesker Nano 36 systemat a rate of 0.5 Å s^{-1} for the first 30 nm and 1.5 Å s^{-1} for the remaining 250 nm at a base pressure lower than 2×10^6 mbar.

Device Characterization. All device characterization was performed under ambient conditions. Current−voltage characteristics were recorded using a Keithley 2636 source meter. The spectral characterization was carried out by illuminating the devices with a Newport Cornerstone 260 monochromator, modulated by a 20 Hz chopper, and monitoring the short-circuit current with a Stanford Research System SR830 apparatus. Over 200 spectrum traces were acquired and averaged for each measurement to avoid out-of-phase noise artifacts. The power of the monochromator was measured in intervals of 2 h with a set of Newport 818IR/UV reference photodetectors. Time-modulated illumination was achieved with a four-channel Thorlabs laser (406 nm source) controlled by an Agilent 33220A waveform generator or alternatively with a NKT Photonics supercontinuum laser source (640 and 900

nm sources) and recorded with an Agilent B1500A semiconductor parameter analyzer or a Keithley 2636 source measurement unit. The photocurrent power dependence was acquired under short-circuit conditions with a Stanford Research System SR830 apparatus under 635 nm diode laser illumination from a Newport (LQA635−08C) apparatus ontrolled by an Agilent 33220A waveform generator.

Device Modeling. Finite-difference time-domain simulations (FDTD) were carried out using Lumerical FDTD solutions suite version 8 (http://www.lumerical.com). A unit cell illuminated with a plane-wave source was simulated with symmetric and antisymmetric boundary conditions. The metal electrode refractive index was taken from Johnson and Christy, and the absorbing ITO was built from absorption measurements using Kramers−Kronig relations. (See Supporting Information section S3 for more details.)

ASSOCIATED CONTENT

Ⓢ Supporting Information

Figures illustrating the role of the alumina layer in the electronic properties of the photodetectors, the fabrication procedure of the quasi-3D plasmonic crystals, FDTD simulations of the plasmonic crystal architecture and LSPR modes sustained by the Au pillars, the metal absorption dependence with the angle of incidence, barrier height estimation, a theoretical model for bias-dependent hot-electron injection, the estimation of the internal quantum efficiency, the study of the dynamic range of the PC based photodetectors, and a performance comparison with other technologies. The Supporting Information is available free of charge on the ACS Publications website at DOI: 10.1021/acsphotonics.5b00149.

AUTHOR INFORMATION

Corresponding Authors
*E-mail: agustin.mihi@icfo.es.
*E-mail: gerasimos.konstantatos@icfo.es.

Author Contributions
F.P.G.A. and A.M. contributed equally to the creation of this work.

Notes
The authors declare no competing financial interest.

ACKNOWLEDGMENTS

REFERENCES

(1) Brolo, A. G. Plasmonics for Future Biosensors. *Nat. Photonics* **2012**, *6*, 709−713.
(2) Baffou, G.; Quidant, R. Nanoplasmonics for Chemistry. *Chem. Soc. Rev.* **2014**, *43*, 3898−3907.
(3) Tokel, O.; Inci, F.; Demirci, U. Advances in Plasmonic Technologies for Point of Care Applications. *Chem. Rev.* **2014**, *114*, 5728−5752.

(4) O'Connor, D.; Zayats, A. V. Data Storage: The Third Plasmonic Revolution. *Nat. Nanotechnol.* **2010**, *5*, 482−483.
(5) Kauranen, M.; Zayats, A. V. Nonlinear Plasmonics. *Nat. Photonics* **2012**, *6*, 737−748.
(6) Geiselmann, M.; Juan, M. L.; Renger, J.; Say, J. M.; Brown, L. J.; de Abajo, F. J. G.; Koppens, F.; Quidant, R. Three-Dimensional Optical Manipulation of a Single Electron Spin. *Nat. Nanotechnol.* **2013**, *8*, 175−179.
(7) Atwater, H. A.; Polman, A. Plasmonics for Improved Photovoltaic Devices. *Nat. Mater.* **2010**, *9*, 205−213.
(8) Konstantatos, G.; Sargent, E. H. Nanostructured Materials for Photon Detection. *Nat. Nanotechnol.* **2010**, *5*, 391−400.
(9) Fei Guo, C.; Sun, T.; Cao, F.; Liu, Q.; Ren, Z. Metallic Nanostructures for Light Trapping in Energy-Harvesting Devices. *Light: Sci. Appl.* **2014**, *3*, e161.
(10) Sze, S. M. *Physics of Semiconductor Devices*, 2nd ed.; John Wiley & Sons: New York, 1981.
(11) Tian, Y.; Tatsuma, T. Plasmon-Induced Photoelectrochemistry at Metal Nanoparticles Supported on Nanoporous TiO_2. *Chem. Commun. (Cambridge, U.K.)* **2004**, 1810−1811.
(12) Nishijima, Y.; Ueno, K.; Yokota, Y.; Murakoshi, K.; Misawa, H. Plasmon-Assisted Photocurrent Generation from Visible to Near-Infrared Wavelength Using a Au-Nanorods/TiO_2 Electrode. *J. Phys. Chem. Lett.* **2010**, *1*, 2031−2036.
(13) Wang, F.; Melosh, N. A. Plasmonic Energy Collection through Hot Carrier Extraction. *Nano Lett.* **2011**, *11*, 5426−5430.
(14) Reineck, P.; Lee, G. P.; Brick, D.; Karg, M.; Mulvaney, P.; Bach, U. A Solid-State Plasmonic Solar Cell via Metal Nanoparticle Self-Assembly. *Adv. Mater.* **2012**, *24*, 4750−4755.
(15) García de Arquer, F. P.; Mihi, A.; Kufer, D.; Konstantatos, G. Photoelectric Energy Conversion of Plasmon-Generated Hot Carriers in Metal-Insulator-Semiconductor Structures. *ACS Nano* **2013**, *7*, 3581−3588.
(16) Mubeen, S.; Lee, J.; Singh, N.; Krämer, S.; Stucky, G. D.; Moskovits, M. An Autonomous Photosynthetic Device in Which All Charge Carriers Derive from Surface Plasmons. *Nat. Nanotechnol.* **2013**, *8*, 247−251.
(17) Mubeen, S.; Lee, J.; Lee, W.-R.; Singh, N.; Stucky, G. D.; Moskovits, M. On the Plasmonic Photovoltaic. *ACS Nano* **2014**, *8*, 6066−6073.
(18) Lee, H.; Lee, Y. K.; Hwang, E.; Park, J. Y. Enhanced Surface Plasmon Effect of Ag/TiO_2 Nanodiodes on Internal Photoemission. *J. Phys. Chem. C* **2014**, *118*, 5650−5656.
(19) García de Arquer, F. P.; Mihi, A.; Konstantatos, G. Molecular Interfaces for plasmonic−hot Electron Photovoltaics. *Nanoscale* **2015**, *7*, 2281−2288.
(20) Knight, M. W.; Sobhani, H.; Nordlander, P.; Halas, N. J. Photodetection with Active Optical Antennas. *Science* **2011**, *332*, 702−704.
(21) Lee, Y. K.; Jung, C. H.; Park, J.; Seo, H.; Somorjai, G. A.; Park, J. Y. Surface Plasmon-Driven Hot Electron Flow Probed with Metal-Semiconductor Nanodiodes. *Nano Lett.* **2011**, *11*, 4251−4255.
(22) Mubeen, S.; Hernandez-Sosa, G.; Moses, D.; Lee, J.; Moskovits, M. Plasmonic Photosensitization of a Wide Band Gap Semiconductor: Converting Plasmons to Charge Carriers. *Nano Lett.* **2011**, *11*, 5548−5552.
(23) Wang, F.; Melosh, N. A. Power-Independent Wavelength Determination by Hot Carrier Collection in Metal-Insulator-Metal Devices. *Nat. Commun.* **2013**, *4*, 1711.
(24) Sobhani, A.; Knight, M. W.; Wang, Y.; Zheng, B.; King, N. S.; Brown, L. V.; Fang, Z.; Nordlander, P.; Halas, N. J. Narrowband Photodetection in the near-Infrared with a Plasmon-Induced Hot Electron Device. *Nat. Commun.* **2013**, *4*, 1643.
(25) Giugni, A.; Torre, B.; Toma, A.; Francardi, M.; Malerba, M.; Alabastri, A.; Proietti Zaccaria, R.; Stockman, M. I.; Di Fabrizio, E. Hot-Electron Nanoscopy Using Adiabatic Compression of Surface Plasmons. *Nat. Nanotechnol.* **2013**, *8*, 845−852.

(26) Chalabi, H.; Schoen, D.; Brongersma, M. L. Hot-Electron Photodetection with a Plasmonic Nanostripe Antenna. *Nano Lett.* **2014**, *14*, 1374−1380.

(27) Li, W.; Valentine, J. Metamaterial Perfect Absorber Based Hot Electron Photodetection. *Nano Lett.* **2014**, *14*, 3510−3514.

(28) Gong, T.; Munday, J. N. Angle-Independent Hot Carrier Generation and Collection Using Transparent Conducting Oxides. *Nano Lett.* **2015**, *15*, 147−152.

(29) Mukherjee, S.; Libisch, F.; Large, N.; Neumann, O.; Brown, L. V.; Cheng, J.; Lassiter, J. B.; Carter, E. A.; Nordlander, P.; Halas, N. J. Hot Electrons Do the Impossible: Plasmon-Induced Dissociation of H$_2$ on Au. *Nano Lett.* **2013**, *13*, 240−247.

(30) Sheldon, M. T.; van de Groep, J.; Brown, A. M.; Polman, A.; Atwater, H. A. Plasmoelectric Potentials in Metal Nanostructures. *Science* **2014**, *346*, 828−831.

(31) Clavero, C. Plasmon-Induced Hot-Electron Generation at Nanoparticle/metal-Oxide Interfaces for Photovoltaic and Photocatalytic Devices. *Nat. Photonics* **2014**, *8*, 95−103.

(32) Marchuk, K.; Willets, K. A. Localized Surface Plasmons and Hot Electrons. *Chem. Phys.* **2014**, *445*, 95−104.

(33) Brongersma, M. L.; Halas, N. J.; Nordlander, P. Plasmon-Induced Hot Carrier Science and Technology. *Nat. Nanotechnol.* **2015**, *10*, 25−34.

(34) Pimpin, A.; Srituravanich, W. Review on Micro- and Nanolithography Techniques and Their Applications. *Eng. J.* **2012**, *16*, 37−56.

(35) Stewart, M. E.; Mack, N. H.; Malyarchuk, V.; Soares, J. A. N. T.; Lee, T.-W.; Gray, S. K.; Nuzzo, R. G.; Rogers, J. A. Quantitative Multispectral Biosensing and 1D Imaging Using Quasi-3D Plasmonic Crystals. *Proc. Natl. Acad. Sci. U.S.A.* **2006**, *103*, 17143−17148.

(36) Chanda, D.; Shigeta, K.; Truong, T.; Lui, E.; Mihi, A.; Schulmerich, M.; Braun, P. V.; Bhargava, R.; Rogers, J. A. Coupling of Plasmonic and Optical Cavity Modes in Quasi-Three-Dimensional Plasmonic Crystals. *Nat. Commun.* **2011**, *2*, 479.

(37) Stewart, M. E.; Mack, N. H.; Malyarchuk, V.; Soares, J. A. N. T.; Lee, T.-W.; Gray, S. K.; Nuzzo, R. G.; Rogers, J. A. Quantitative Multispectral Biosensing and 1D Imaging Using Quasi-3D Plasmonic Crystals. *Proc. Natl. Acad. Sci. U.S.A.* **2006**, *103*, 17143−17148.

(38) Meinzer, N.; Barnes, W. L.; Hooper, I. R. Plasmonic Meta-Atoms and Metasurfaces. *Nat. Photonics* **2014**, *8*, 889−898.

(39) Xia, Y.; Whitesides, G. M. Soft Lithography. *Annu. Rev. Mater. Sci.* **1998**, *28*, 153−184.

(40) Ferry, V. E.; Verschuuren, M. A.; Li, H. B. T.; Schropp, R. E. I.; Atwater, H. A.; Polman, A. Improved Red-Response in Thin Film a-Si:H Solar Cells with Soft-Imprinted Plasmonic Back Reflectors. *Appl. Phys. Lett.* **2009**, *95*, 183503.

(41) Mihi, A.; Beck, F. J.; Lasanta, T.; Rath, A. K.; Konstantatos, G. Imprinted Electrodes for Enhanced Light Trapping in Solution Processed Solar Cells. *Adv. Mater.* **2014**, *26*, 443−448.

(42) García de Abajo, F. J. Colloquium: Light Scattering by Particle and Hole Arrays. *Rev. Mod. Phys.* **2007**, *79*, 1267−1290.

(43) Teperik, T. V.; Popov, V. V.; García de Abajo, F. J.; Abdelsalam, M.; Bartlett, P. N.; Kelf, T. A.; Sugawara, Y.; Baumberg, J. J. Strong Coupling of Light to Flat Metals via a Buried Nanovoid Lattice: The Interplay of Localized and Free Plasmons. *Opt. Express* **2006**, *14*, 1965.

(44) Kelf, T.; Sugawara, Y.; Cole, R.; Baumberg, J.; Abdelsalam, M.; Cintra, S.; Mahajan, S.; Russell, A.; Bartlett, P. Localized and Delocalized Plasmons in Metallic Nanovoids. *Phys. Rev. B* **2006**, *74*, 245415.

(45) Hendry, E.; Garcia-Vidal, F.; Martin-Moreno, L.; Rivas, J. G.; Bonn, M.; Hibbins, A. P.; Lockyear, M. J. Optical Control over Surface-Plasmon-Polariton-Assisted THz Transmission through a Slit Aperture. *Phys. Rev. Lett.* **2008**, *100*, 123901.

(46) Fowler, R. The Analysis of Photoelectric Sensitivity Curves for Clean Metals at Various Temperatures. *Phys. Rev.* **1931**, *38*, 45−56.

(47) Scales, C.; Berini, P. Thin-Film Schottky Barrier Photodetector Models. *IEEE J. Quantum Electron.* **2010**, *46*, 633−643.

(48) Govorov, A. O.; Zhang, H.; Gun'ko, Y. K. Theory of Photoinjection of Hot Plasmonic Carriers from Metal Nanostructures into Semiconductors and Surface Molecules. *J. Phys. Chem. C* **2013**, *117*, 16616−16631.

(49) Zhang, H.; Govorov, A. O. Optical Generation of Hot Plasmonic Carriers in Metal Nanocrystals: The Effects of Shape and Field Enhancement. *J. Phys. Chem. C* **2014**, *118*, 7606−7614.

(50) Govorov, A. O.; Zhang, H.; Demir, H. V.; Gun'ko, Y. K. Photogeneration of Hot Plasmonic Electrons with Metal Nanocrystals: Quantum Description and Potential Applications. *Nano Today* **2014**, *9*, 85−101.

(51) Kanter, H. Slow-Electron Mean Free Paths in Aluminum, Silver, and Gold. *Phys. Rev. B* **1970**, *1*, 522−536.

(52) Manjavacas, A.; Liu, J. G.; Kulkarni, V.; Nordlander, P. Plasmon-Induced Hot Carriers in Metallic Nanoparticles. *ACS Nano* **2014**, *8*, 7630−7638.

(53) Sobhani, A.; Knight, M. W.; Wang, Y.; Zheng, B.; King, N. S.; Brown, L. V.; Fang, Z.; Nordlander, P.; Halas, N. J. Narrowband Photodetection in the near-Infrared with a Plasmon-Induced Hot Electron Device. *Nat. Commun.* **2013**, *4*, 1643.

(54) Casalino, M.; Coppola, G.; Iodice, M.; Rendina, I.; Sirleto, L. Near-Infrared Sub-Bandgap All-Silicon Photodetectors: State of the Art and Perspectives. *Sensors* **2010**, *10*, 10571−10600.

(55) Rogalski, A. HgCdTe Infrared Detector Material: History, Status and Outlook. *Rep. Prog. Phys.* **2005**, *68*, 2267−2336.

(56) Ng, B.; Wu, J.; Hanham, S. M.; Fernández-Domínguez, A. I.; Klein, N.; Liew, Y. F.; Breese, M. B. H.; Hong, M.; Maier, S. A. Spoof Plasmon Surfaces: A Novel Platform for THz Sensing. *Adv. Opt. Mater.* **2013**, *1*, 543−548.

(57) Lehmann, J.; Merschdorf, M.; Pfeiffer, W.; Thon, A.; Voll, S.; Gerber, G. Surface Plasmon Dynamics in Silver Nanoparticles Studied by Femtosecond Time-Resolved Photoemission. *Phys. Rev. Lett.* **2000**, *85*, 2921−2924.